World Electric Vehicle Journal

MDPI

Article

Research on the Smooth Switching Control Strategy of Electric Vehicle Charging Stations Based on Photovoltaic–Storage–Charging Integration

Tao Wang, Jinghao Ma *, Cunhao Lin, Xin Li, Shenhui Chen and Jihui Zhang

Mechanical Engineering, College of Mechanical and Equipment Engineering, New Campus, Hebei University of Engineering, Handan 056038, China; wangtao24@hebeu.edu.cn (T.W.); lch16311@163.com (C.L.); lixinppmn@gmail.com (X.L.); hg702csh@163.com (S.C.); 15893620363@163.com (J.Z.)
* Correspondence: m2403184949@126.com

Abstract: To facilitate seamless transitions between grid-connected and islanded modes in PV–storage–charging integration, an energy storage system converter is designated as the subject of investigation, and its operational principles are examined. Feed-forward decoupling, double closed-loop, constant-power (PQ), constant-voltage–constant-frequency (V/F), and constant-voltage charge and discharge control strategies are developed. The PQ and V/F control framework of the energy storage battery comprises an enhanced common current inner loop and a switching voltage outer loop. The current reference value output by the voltage outer loop and the voltage signal output by the current inner loop are compensated. The transient impact is reduced, and the smooth switching of the microgrid from the grid-connected mode to the island mode is realized, which significantly improves the power quality and ensures the uninterrupted charging of electric vehicles and the stable operation of the key load of the system. By constructing a simulation model of the photovoltaic energy storage microgrid on the MATLAB/Simulink platform, the practicability of the control strategy proposed in this paper is verified.

Keywords: photovoltaic energy storage microgrid; PQ control; V/F control; smooth switching

Citation: Wang, T.; Ma, J.; Lin, C.; Li, X.; Chen, S.; Zhang, J. Research on the Smooth Switching Control Strategy of Electric Vehicle Charging Stations Based on Photovoltaic–Storage–Charging Integration. *World Electr. Veh. J.* **2024**, *15*, 528. https://doi.org/10.3390/wevj15110528

Academic Editor: Vladimir Katic

Received: 6 October 2024
Revised: 13 November 2024
Accepted: 13 November 2024
Published: 17 November 2024

1. Introduction

With the advancement of electric vehicles and the increasingly serious energy crisis and environmental pollution problems, coupled with the increasing awareness of the vulnerability of traditional large-scale power grids, countries around the world are gradually focusing on more environmentally friendly, efficient, and reliable distributed generation technology to maintain the uninterrupted charging process of electric vehicles and improve the service life of electric vehicle batteries. This transformation has promoted the large-scale promotion and application of distributed power technology [1–3]. Due to their increased flexibility and uniqueness, microgrids, which consist of a distributed generation unit, an energy storage unit, a load, and a monitoring and protection device, are frequently employed [4,5]. Microgrids can not only be connected to the large power grid through the public interface but can also quickly disconnect when the distribution network fails, independently supply power to the electric vehicle, and ensure the continuous operation of the key load of the system. Once the large power grid fault is repaired, the microgrid can be connected to the grid again. Therefore, secure and stable microgrid control technology has attracted widespread attention and become the focus of research at home and abroad [6–9].

The inverter, a crucial element of the microgrid, can be categorized into two control modes: master–slave control, which is appropriate for a master–slave configuration, and droop control, which is ideal for a peer-to-peer arrangement [10–12]. Because they are

more vulnerable to environmental effects, paired structures have a lower safety factor and can completely fail if they sustain damage. The master–slave configuration often requires a high-capacity converter as the primary power source to deliver the principal energy supply for the microgrid. Consequently, photovoltaic energy storage microgrids typically employ a master–slave control [13–15]. In grid-connected operations, the main inverter usually uses a PQ control strategy to manage the power output. In the islanded operating mode, this is transitioned to a V/f control to stabilize frequency and voltage [16–18]. The alterations in the control target and influence mechanism will temporarily impact the system's stability and output quality. Consequently, the formulation of a control strategy characterized by high sensitivity and a swift response to mode transitions is crucial for ensuring the smoothness and safety of microgrid operations [19–22]. A multitude of domestic and international researchers have examined the issues arising from mode switching. In Reference [23], by modifying the combination of the current controller and voltage regulator in the main inverter of the microgrid system, the voltage threshold during unplanned islanding detection is circumvented. However, since the output of the voltage outer loop and the additional current loop are input into the current inner loop together, the calculation process is complicated, and its dynamic and transient stability needs to be further improved. In Reference [24], a hybrid energy storage unit is used as the main controller to control the voltage phase during the off-grid process, and droop control is used to realize the undifferentiated tracking control of the voltage phase and the amplitude of the common coupling point during the grid-connected process, which suppresses the system oscillations caused by the switching process. In Reference [25], an error feedback mechanism is incorporated into the droop control loop, and a virtual impedance is integrated into the conventional droop control to render the inverter's output impedance resistive, thereby facilitating the seamless transition of the low-voltage microgrid. In Reference [26], the pre-synchronization module is incorporated into the phase-locked loop to rectify the phase discrepancy between the microgrid feeder and the grid, while pre-calculation is integrated into the voltage loop. However, there is still a large current overshoot during the switching process. In Reference [27], PQ control and V/F control are combined, the voltage outer loop is combined with the current inner loop, and the output of the voltage outer loop is compensated. Additionally, a synchronous control is added, which effectively reduces the transient impact. However, only the voltage outer loop is compensated, and the current inner loop is not improved. In Reference [28], the author suggests the use of a smooth switching control rate and uses the technique of cutting off the load in the c-region, where the situation is critical, after examining the amplitude–frequency characteristics and time domain of the controller's transfer function [29]. In Reference [30], a disturbance observer is used to track abrupt currents and create an equivalent disturbance to compensate for the current inner loop in order to address the issue of a transient overcurrent and overvoltage in MMC-PET under grid-connected and off-grid mode switching. This ensures that the mutation current is inhibited. However, the disturbance observer's gain coefficient requires further optimization because it is influenced by several parameters, such as line impedance, operating conditions, and voltage level. In Reference [31], through the implementation of the Van der Pol virtual oscillation controller and PQ control coordinated control method, each power generation unit has a high synchronization speed, strong current sharing performance, and good dynamic characteristics. By contrasting this control method with the conventional droop control, the superiority of this system is demonstrated. LPF should be included when amplitude synchronization is carried out because it is too difficult to achieve this control due to its intricate computation. As a result, the controller is rather rigid. In References [32,33], the adaptive fuzzy directional bat algorithm solves this problem by not requiring optimization of the initial parameters. This approach is used for an adaptive protection system in the microgrid environment, taking into account the connection state of the distributed generator set in various scenarios. It is more reliable and responds more quickly than the conventional protective system. Its trip time is significantly shortened in island mode. It is noted that, in the

future, microgrids will unavoidably rely on dynamic and adaptable solutions. Therefore, this paper takes a small electric vehicle charging station as a microgrid system and adopts an improved smooth switching control strategy. It does not need to remove the excess load, so the current impact and frequency fluctuations in the microgrid system are reduced when the grid-connected mode is converted to the off-grid mode, which avoids interruptions to the charging process of the electric vehicle and improves the service life of the energy storage battery.

This study provides a detailed introduction to the structure of photovoltaic energy storage microgrids and analyzes two primary control mechanisms for energy storage system inverters: constant power control (PQ control strategy) and constant voltage constant frequency control (V/F control strategy). In grid-connected operation mode, fluctuations in PV output power may impact the stability of the common coupling point voltage (PCC). A control method based on PCC bus voltage is therefore formulated. By regulating the energy storage battery to absorb and inject varying power levels, the AC bus voltage is sustained within the permissible fluctuation range. Upon transitioning from grid-connected mode to island mode, the photovoltaic inverter consistently employs PQ control to maximize output power, and the voltage and frequency cannot be adjusted. Consequently, the energy storage inverter must be transitioned to V/F control to ensure steady frequency and voltage for the microgrid system. This research also examines the factors contributing to bus voltage and current oscillations during the transition of the photovoltaic energy storage microgrid from grid-connected mode to island mode. In this paper, a smooth switching control strategy with voltage and current compensation is adopted. Compared with the hard switching of PQ control and V/F control, the switching of the current inner loop is reduced, and the control method of only switching the voltage outer loop and sharing the current inner loop is adopted. Compared with the traditional smooth switching control strategy, the voltage outer loop and the current inner loop are compensated, which reduces the sudden change in the reference current generated during the switching process of the voltage outer loop and the impact of the reference voltage output by the current inner loop on the inverter. The transient impact generated from the grid-connected mode to the island mode is greatly reduced. Finally, the simulation model of the photovoltaic energy storage microgrid system is established using MATLAB software to validate the control approach presented in this paper.

This paper presents a thorough analysis of the scheme discussed in the preceding section. Initially, Section 2 establishes the framework of a photovoltaic energy storage microgrid. In Section 3, a mathematical model and analysis of a bidirectional DC/DC converter, as well as a three-phase voltage source PWM converter, are presented. Section 4 introduces a feedforward decoupling-based double closed-loop control method for regulating voltage and current in the three-phase voltage source PWM converter, accompanied by a PQ control technique. The control strategy for the energy storage battery is enhanced through the implementation of a smooth switching control approach that employs a common current inner loop and a switching voltage outer loop. The efficacy of the proposed control method is demonstrated in Section 5 through the development of a simulation model utilizing MATLAB/Simulink and verified by experiments.

2. Photovoltaic Energy Storage Microgrid Structure

Figure 1 is the topology of the photovoltaic energy storage microgrid used in this paper.

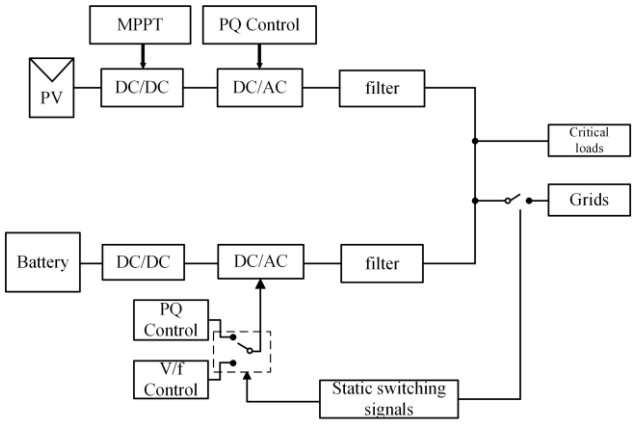

Figure 1. Photovoltaic energy storage microgrid topology.

In this configuration, the photovoltaic panel is connected to the voltage source inverter via a unidirectional DC/DC converter, which is subsequently subjected to filtering through an L-type filter. Concurrently, the battery interfaces with the AC/DC converter through a bidirectional DC/DC converter, which is filtered using an LC-type filter. At the PCC, the solar energy generation system and the energy storage system converge to establish a connection to the grid. The photovoltaic system operates continuously at its maximum power output, employing PQ control for its inverter. When the energy storage system operates in grid-connected mode, its inverter also utilizes PQ control, managing the charging and discharging of the battery by monitoring the power at the common coupling point in conjunction with the requisite grid-connected power. In instances where the microgrid becomes disconnected from the main grid, the energy storage system transitions to V/F control to maintain stable voltage and frequency levels within the microgrid. The control strategy shifts from PQ to V/F control during the transition of the photovoltaic energy storage system from grid-connected to off-grid operation. Although both control strategies utilize an identical current control loop, they differ in their front-end inputs. Consequently, fluctuations in current and voltage are anticipated during the switching process, resulting in variations in the system's frequency and power output.

3. The Establishment of a Mathematical Model of Photovoltaic Energy Storage Microgrid Systems

3.1. Three-Phase PWM Rectifier Structure and Mathematical Model

The three-phase voltage source PWM inverter is comprised of six power switches organized in a symmetrical configuration on the AC side. This system exhibits significant coupling characteristics and demonstrates nonlinearity. The six power switch devices operate complementarily between the upper and lower half bridges, utilizing SVPWM technology to regulate the switching signals, designated as T_1~T_6, of the power switches.

Figure 2 illustrates the topological configuration of the photovoltaic storage system. U_{PV} is representative of the output voltage generated by the photovoltaic panel. r_1 is representative of the internal resistance associated with the photovoltaic panel. E_{bat} represents the output voltage of energy storage battery. r_2 is representative of the internal resistance associated with an energy storage battery. C_1 and C_2 are DC-side voltage stabilized capacitors. L_1 and L_2 are DC-side inductors. C and C_3 are output filter capacitors. L and L_3 are AC-measured filter inductors. R_1 and R_2 are line resistances. C_4 is an AC filter capacitor.

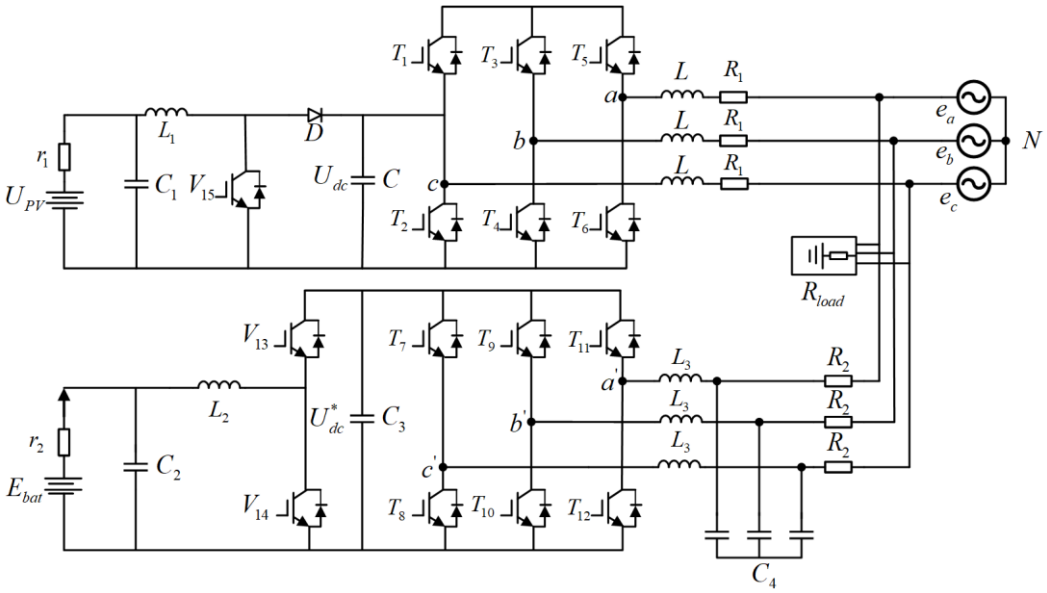

Figure 2. Diagram of the photovoltaic energy storage system's main circuit topology.

The mathematical modeling of a photovoltaic system within a three-phase stationary coordinate system can be developed through the application of Kirchhoff's voltage law.

$$L\frac{d}{dt}\begin{bmatrix} i_a \\ i_b \\ i_c \end{bmatrix} = \begin{bmatrix} e_a \\ e_b \\ e_c \end{bmatrix} - R_1\begin{bmatrix} i_a \\ i_b \\ i_c \end{bmatrix} - \begin{bmatrix} u_a \\ u_b \\ u_c \end{bmatrix} \tag{1}$$

In Formula (1), i_a, i_b, and i_c are the three-phase current of the inverter output side, respectively. u_a, u_b, and u_c are the phase voltages that connect the inverter's output to the grid voltage at its neutral point N. e_a, e_b, and e_c are the grid voltages. L is the output side filter inductance of the photovoltaic inverter. R_1 is the line equivalent resistance.

From Formula (1), it is evident that there exists no coupling relationship between the AC side voltage and current; however, these parameters exhibit temporal variations. To mitigate the complexity of system control and enhance both the response speed and stability, the Clarke transformation can be employed to convert the three-phase system into two orthogonal components, specifically the α–β coordinate system. Subsequently, the Park transformation is utilized to derive a two-phase synchronous rotating coordinate system from the two-phase stationary coordinate system, resulting in the d–q coordinate system. This transformation effectively converts the three-phase alternating current into two DC components, thereby facilitating the implementation of the control strategy.

Formula (1) can be converted into the α–β coordinate system through the subsequent relationship.

$$\begin{bmatrix} x_\alpha \\ x_\beta \end{bmatrix} = \frac{2}{3}\begin{bmatrix} 1 & -\frac{1}{2} & -\frac{1}{2} \\ 0 & \frac{\sqrt{3}}{2} & -\frac{\sqrt{3}}{2} \end{bmatrix}\begin{bmatrix} x_a \\ x_b \\ x_c \end{bmatrix} \tag{2}$$

In Formula (2), x_α and x_β represent the two-phase components within the α–β coordinate system respectively. x_a, x_b, and x_c represent the components in the three-phase stationary coordinate system, respectively.

Formula (3) is derived from Formulas (1) and (2):

$$L\frac{d}{dt}\begin{bmatrix} i_\alpha \\ i_\beta \end{bmatrix} = \begin{bmatrix} e_\alpha \\ e_\beta \end{bmatrix} - R_1\begin{bmatrix} i_\alpha \\ i_\beta \end{bmatrix} - \begin{bmatrix} u_\alpha \\ u_\beta \end{bmatrix} \tag{3}$$

In Formula (3), the components of the solar inverter's output current in the α–β coordinate system are denoted by i_α and i_β. e_α and e_β are the components of the grid voltage in the α–β coordinate system. In the α–β coordinate system, u_α and u_β are the parts of the photovoltaic inverter's output side voltage.

Through Formula (4), Formula (3) can be transformed into the d–q rotating coordinate system:

$$\begin{bmatrix} x_d \\ x_q \end{bmatrix} = \begin{bmatrix} \cos\omega t & \sin\omega t \\ -\sin\omega t & \cos\omega t \end{bmatrix}\begin{bmatrix} x_\alpha \\ x_\beta \end{bmatrix} \tag{4}$$

In Formula (4), x_d and x_q represent two DC components in the d–q rotating coordinate. ω is the angular velocity with which the coordinate axis rotates. t is time.

Substituting Formula (3) into Formula (4), the photovoltaic system's mathematical model in d–q coordinate system may be acquired:

$$L\frac{d}{dt}\begin{bmatrix} i_d \\ i_q \end{bmatrix} = \begin{bmatrix} e_d \\ e_q \end{bmatrix} - R_1\begin{bmatrix} i_d \\ i_q \end{bmatrix} - \begin{bmatrix} u_d \\ u_q \end{bmatrix} + \omega L\begin{bmatrix} i_q \\ -i_d \end{bmatrix} \tag{5}$$

In Formula (5), the components of the solar inverter's output side current in the d–q coordinate system are i_d and i_q, respectively. e_d, e_q is the component of grid voltage in the d–q coordinate system. u_d, u_q represents the component of the output side voltage of the photovoltaic inverter in the d–q coordinate system.

3.2. Bidirectional DC/DC Converter

In the field of power electronics, a bidirectional DC/DC converter is a device engineered to facilitate the conversion of DC voltage in both directions. This apparatus allows for both step-up and step-down voltage conversions through the modulation of its power diode's operation. Furthermore, it adjusts the output voltage in response to variations in demand [34].

When the battery undergoes discharge, the bidirectional DC/DC converter functions analogously to a boost chopper circuit. Utilizing Kirchhoff's voltage law, one can derive Formula (6):

$$L_2\frac{di_1}{dt} + r_2 i_2 + E_{bat} = 0 \tag{6}$$

In Formula (6), i_2 is the battery output current. E_{bat} is the equivalent electromotive force of the battery. The battery's internal resistance is equal to r_2. L_2 is an inductance.

The value of i_2 in Formula (6) is obtained by the three-element method. When the power switch T_{14} is disconnected, the output current of the battery reaches the maximum value I_{20}:

$$\begin{cases} i_2 = I_{10}e^{-\frac{t}{\tau}} + \dfrac{E_{bat}}{r_2}(1-e^{-\frac{t}{\tau}}) \\ i_{20} = I_{10}e^{-\frac{t_{on}}{\tau}} + \dfrac{E_{bat}}{r_2}(1-e^{-\frac{t_{on}}{\tau}}) \end{cases} \tag{7}$$

In Formula (7), τ is a function of time, $\tau = L/R$. I_{10} is the current value when the power switch tube T_{14} is on. t_{on} is the moment at which the power switch is turned on.

When T_{14} is disconnected, the inductor L_2 is used as the energy storage element to store the current, and the current reaches the maximum value. According to the Kirchhoff voltage law:

$$L_2 \frac{di_1}{dt} + r_2 i_2 + E_{bat} = U_{dc}^* \tag{8}$$

In Formula (8), the energy storage system's DC bus voltage is denoted as U_{dc}^*.

The value of i_1 in Formula (8) is obtained by the three-element method. When the power switch T_{13} is disconnected, the value of i_2 is the initial current value I_{10}.

$$\begin{cases} i_2 = I_{20} e^{-\frac{t_{off}}{\tau}} + \dfrac{U_{dc}^* - E_{bat}}{r_d}(1 - e^{-\frac{t_{off}}{\tau}}) \\ I_{10} = I_{20} e^{-\frac{t_{off}}{\tau}} + \dfrac{U_{dc}^* - E_{bat}}{r_d}(1 - e^{-\frac{t_{off}}{\tau}}) \end{cases} \tag{9}$$

In Formula (9), t_{off} denotes the deactivation time of the power switch.

Combining Formulas (7) and (9), we can obtain:

$$U_{dc}^* = \frac{t_{on} + t_{off}}{t_{off}} E_{bat} = \frac{T}{t_{off}} E_{bat} = \frac{1}{1 - \alpha} E_{bat} \tag{10}$$

When $T / t_{off} \geq 1$, battery discharge occurs when the bidirectional DC/DC converter functions in boost mode. The computational processes involved in this phenomenon are similar to those previously outlined, as the principles that govern the charging and discharging of batteries remain fundamentally consistent.

$$U_{dc}^* = \frac{t_{on}}{t_{on} + t_{off}} E_{bat} = \frac{t_{on}}{T} E_{bat} = \alpha E_{bat} \tag{11}$$

In particular, $T / t < 1$ represents a reduced operational state during which the battery is in the process of charging.

3.3. Implementation of a PWM Converter Control Technique for a Three-Phase Voltage Source

Under standard operational conditions, a total of four power units are produced. The output power of the photovoltaic system is P_{pv}, the output power of the battery is P_{bat}, the power of the important load is P_{load}, and the output power of the grid is P_{grid}.

3.3.1. When the Photovoltaic Energy Storage System Is Connected to the Grid

$$P_{pv} + P_{bat} - P_{load} - P_{grid} = 0 \tag{12}$$

In Formula (12), the photovoltaic system functions as the principal source of energy generation, operating in a positive state. In contrast, the energy storage battery demonstrates a positive state during the discharge phase and a negative state during the charging phase. The significant load serves as the regulator within the photovoltaic energy storage system, progressively utilizing active power. It is essential to emphasize that the power consumed by the load is less than the power generated by the photovoltaic system.

The operational status of the battery can be assessed by examining the interrelationship among the four components.

1. When $P_{pv} > P_{grid} + P_{load}$, $P_{bat} < 0$, $P_{pv} = P_{grid} + P_{load} - P_{bat}$, the energy storage battery is in the charging state, the bidirectional DC/DC converter is in the step-down state, and the state of charge of the energy storage battery increases.
2. When $P_{pv} < P_{grid} + P_{load}$, $P_{bat} > 0$, $P_{pv} + P_{bat} - P_{load} = P_{grid}$, the energy storage battery is in the discharge state, the bidirectional DC/DC converter is in the boost state, and the state of charge of the energy storage battery is reduced.

3. When $P_{pv} = P_{bat} + P_{load}$, $P_{bat} = 0$, the state of charge of the energy storage battery remains unchanged.

3.3.2. When the Photovoltaic Energy Storage System Is in Off-Grid Operation

$$P_{pv} + P_{bat} - P_{load} = 0 \tag{13}$$

In Formula (13), the inter-relationship among the three components demonstrates that when the output power generated by the photovoltaic system exceeds the power consumed by the load, the energy storage battery enters a charging state, thereby absorbing the surplus power. During this phase, the bidirectional DC/DC converter functions in buck mode, resulting in an increase in the state of charge of the energy storage battery. Conversely, when the output power of the photovoltaic system is inadequate to satisfy the load demand, the energy storage battery discharges, entering a discharge state. In this scenario, the bidirectional DC/DC converter operates in boost mode, which leads to a decrease in the state of charge of the energy storage battery.

4. Grid-Connected and the Off-Grid Control Strategy of Photovoltaic Energy Storage Systems

4.1. Modulation Technique for PV System PWM Converters with Three-Phase Input Voltages

The three-phase voltage source PWM converter utilized in solar energy systems employs a dual closed-loop control strategy for the regulation of voltage and current. To ensure synchronization between the input and the grid in terms of both phase and frequency, PLL technology is employed to extract phase information from the grid voltage. The output from the outer voltage control loop serves as the input for the inner current control loop. Subsequently, a pulse signal is generated and transmitted to six power switches through the application of SVPWM techniques.

Figure 3 illustrates the control block diagram relevant to the inverter in a photovoltaic system.

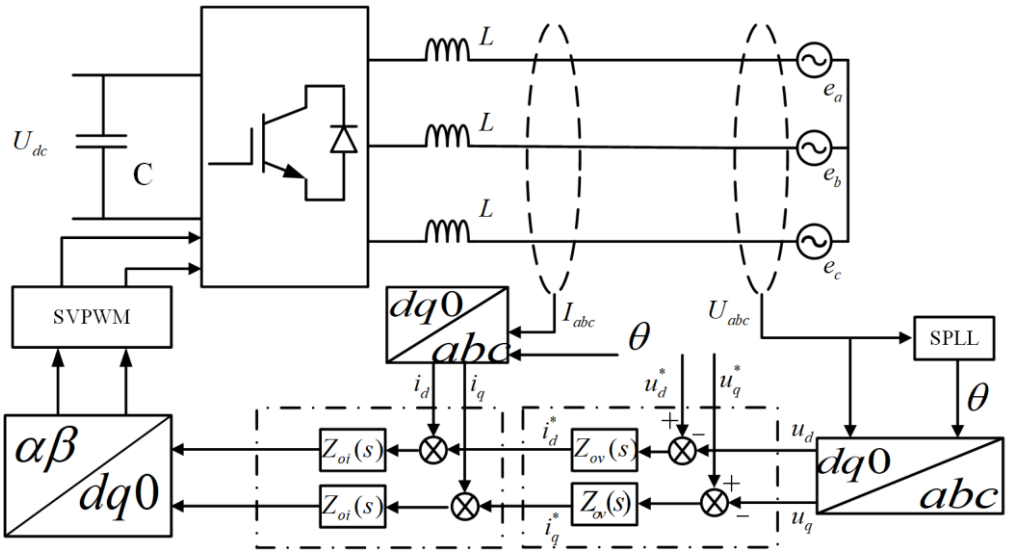

Figure 3. Inverter control block diagram in the photovoltaic system.

From Formula (5), it is apparent that the d-axis and q-axis components of the photovoltaic system demonstrate a coupling relationship within the two-phase rotating coordinate system, commonly known as the *d*–*q* coordinate system. Typically, decoupling control is implemented through a control methodology that utilizes feedforward decoupling. To enable the independent control of direct current (DC) variables, a PI regulator is

employed as the current controller. As a result, the current differential term presented in Formula (5) can be derived:

$$\begin{cases} u_d = -\left(K_{iP} + \dfrac{K_{iI}}{s}\right)\left(i_d^* - i_d\right) + \omega L i_q + e_d \\ u_q = -\left(K_{iP} + \dfrac{K_{iI}}{s}\right)\left(i_q^* - i_q\right) - \omega L i_d + e_q \end{cases} \tag{14}$$

In Formula (14), K_{iP} and K_{iI} represent the proportional and integral regulation gains of the current inner control loop, respectively. S is the complex frequency domain. Bring Formula (14) into Formula (5):

$$\begin{cases} L\dfrac{di_d}{dt} = \left(K_{iP} + \dfrac{K_{iI}}{s}\right)\left(i_d^* - i_d\right) \\ L\dfrac{di_q}{dt} = \left(K_{iP} + \dfrac{K_{iI}}{s}\right)\left(i_q^* - i_q\right) \end{cases} \tag{15}$$

From Formula (15), it is feasible to derive the equation governing the decoupled current loop control. The current loop of a grid-connected inverter can be decoupled by employing feedforward decoupling techniques.

Figure 4 presents the current loop control block diagram.

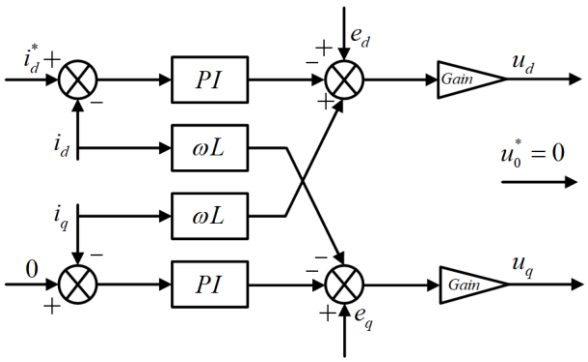

Figure 4. Design of the control loop for the feedforward decoupling of grid voltage and current.

The research presented indicates that the existing inner loop effectively reduces voltage fluctuations following d-axis decoupling by improving the dynamic response speed of the control process. Figure 5 depicts the transfer block diagram of the decoupled current loop in the d-axis.

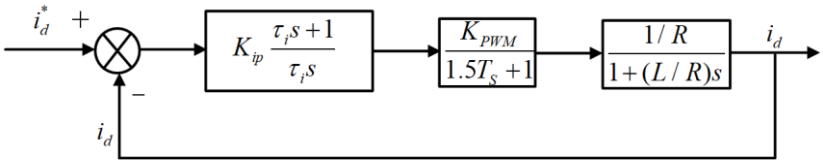

Figure 5. Control block schematic of the current loop.

In Figure 5, K_{ip} is the proportional regulation gain of the current inner loop. i_d^* is the d-axis reference component of the AC side voltage vector of the three-phase voltage source inverter. K_{PWM} stands for the inverter's equivalent gain. T_s stands for the inverter's switching duration. $1/1.5T_s+1$ stands for the sampling signal delay. To facilitate the calculation, the time constant T_s and the time constant $0.5T_s$ of the small inertial link are combined to obtain $1.5T_s$. For the PI regulator, $G_{PI}(s)$ stands for the transfer

function, the time constant is τ_i, and the value is $K_{iP}/K_{iI} = L/R$. One way to find the current loop's transfer Formula (16) $G_{PI}(s)$ is:

$$G_{PI}(s) = K_{ip}\frac{\tau_i + 1}{\tau_i + s} \tag{16}$$

In Figure 5, we can see the open-loop transfer Formula (17):

$$G(s) = G_{PI}(s)\cdot\frac{K_{PWM}}{1.5T_S + 1}\cdot\frac{1}{sL + R} \tag{17}$$

To improve the followability of the current inner loop regulator, it may be designed in accordance with the conventional type I system. Based on this evaluation, it is feasible to derive the closed-loop transfer Formula (18) $Z_{ci}(s)$:

$$\begin{aligned} Z_{ci}(s) &= \frac{G(s)}{G(s)+1} = \frac{1}{1+\frac{R\tau_i}{K_{iP}K_{PWM}}s + \frac{1.5T_sR\tau_i}{K_{iP}K_{PWM}}s^2} \\ &= \frac{1}{1+\frac{L}{K_{iP}K_{PWM}}S + \frac{1.5LT_s}{K_{iP}K_{PWM}}s^2} \end{aligned} \tag{18}$$

In Formula (19), when the damping ratio of the system is represented as $\xi = 0.707$, it is possible to derive the following results from the parameter tuning relationship characteristic of a standard Type I system:

$$\frac{1.5T_sK_{iP}K_{PWM}}{R\tau_i} = \frac{1}{2} \tag{19}$$

The formula for the control parameters of the current inner loop PI regulator can be located in Formula (20):

$$\begin{cases} K_{iP} = \dfrac{R\tau_i}{3T_sK_{PWM}} \\ K_{iI} = \dfrac{R}{3T_sK_{PWM}} \end{cases} \tag{20}$$

After calculation, $K_{ip} = 5$, $K_{iI} = 300$ is obtained.

The primary objective of the voltage outer loop is to ensure the stability of the DC side voltage in a three-phase voltage source PWM rectifier. Therefore, it is essential to highlight the robustness of the voltage loop in mitigating interference during the regulation of the control system. A conventional type II control system is deemed appropriate for the design of the voltage regulator.

In Figure 6, C is the DC side capacitor. K_{vp} and K_{vI} are the parameters of the voltage outer loop PI regulator, respectively. u_{dc}^* is the DC side voltage reference value. τ_v is the small inertia time constant of voltage outer loop sampling. $Z_{ci}(s)$ is the transfer function of the current inner loop. m represents the modulation ratio of pulse width modulation (PWM). θ represents the initial phase angle of the fundamental wave associated with the switching function. i_L represents the electric current that passes through the inductor.

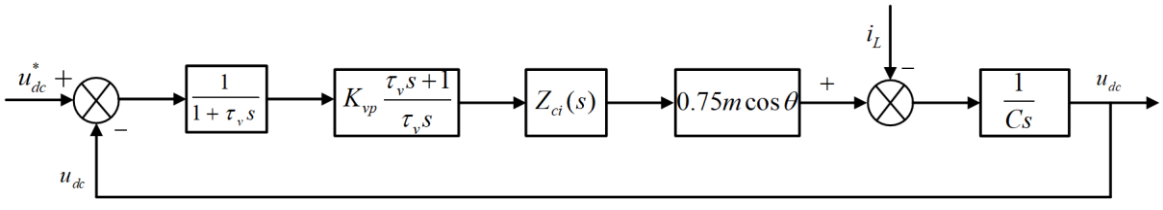

Figure 6. Voltage loop control block diagram.

The analysis suggests that the equivalent transfer function of the inner current loop is denoted as $Z_{ci}(s)=1/(1+3T_s s)$. The regulation of the outer voltage loop is characterized by time-varying dynamics, which poses a considerable challenge in the design of the voltage loop. It may be prudent to consider the substitution of the maximum proportional gain within the feedback loop. For $0.75m\cos\theta \le 0.75(m \le 1)$, the optional proportional gain is 0.75. To simplify the control structure, let $T_{ev}=\tau_v+3T_s$.

Formula (21) is the open-loop transfer function of voltage loop:

$$Z_{ov}(s)=\frac{0.75K_v(T_v s+1)}{CT_v s^2(T_{ev}s+1)} \tag{21}$$

Formula (22) is the bandwidth h_v:

$$h_v=\frac{T_v}{T_{ev}} \tag{22}$$

Formula (23) is a typical type II system controller for system parameter tuning:

$$\frac{0.75K_v}{CT_v}=\frac{h_v+1}{2h_v^2T_{ev}^2} \tag{23}$$

Engineers typically choose the intermediate frequency bandwidth by taking into account the anti-interference capabilities and the responsiveness of the voltage loop control system. $h_v=T_v/T_{ev}=5$, taking $h_v=5$ into Formula (23). The parameters of the PI regulator for the voltage loop can be ascertained in Formula (24):

$$\begin{cases} K_{vp}=\dfrac{4C}{5(\tau_v+3T_s)} \\ K_{vI}=\dfrac{4C}{25(\tau_v+3T_s)^2} \end{cases} \tag{24}$$

After calculation, $K_{vP}=1$, $K_{vI}=10$ is obtained.

4.2. Control Strategy of a Bi-Directional DC/DC Converter for Energy Storage Systems

The bi-directional converter utilizes a constant voltage control strategy throughout both the charging and discharging processes. The power switch is activated by a PWM signal, which is generated by a PI regulator. This regulator assesses the difference between the input voltage and the actual output voltage, thereby producing the command value for the battery current along with other outputs. The detailed control methodology is illustrated in Figure 7.

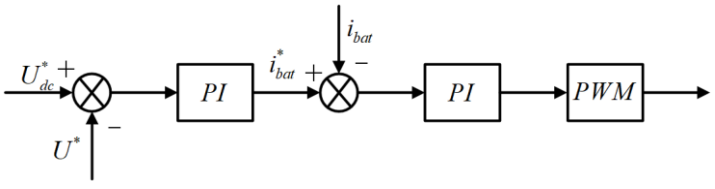

Figure 7. Constant pressure control block diagram.

4.3. Methods for Controlling Energy Storage Inverters When Operating in Grid-Connected Mode

A PQ control system, which primarily consists of a power outer loop, a current inner loop, and a phase-locked loop, is implemented in the post-stage of the energy storage system. The power outer loop control, as depicted in Figure 8 of the PQ control block diagram, is responsible for monitoring and regulating the system's output power, thereby ensuring a consistent delivery of 10,000 W to the grid.

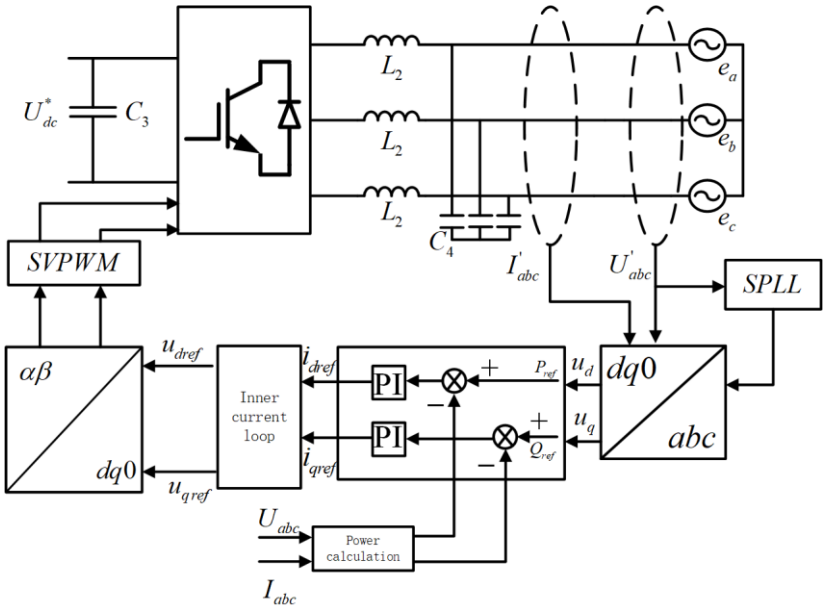

Figure 8. Energy storage system control block schematic for the grid-connected operation mode.

The following formula for calculation is employed within the energy storage system, which continues to utilize PI control:

$$\begin{cases} i_{dref} = \dfrac{3}{2u_d}(K_{pP} + \dfrac{K_{pI}}{s})(P_{ref} - P) \\ i_{qref} = -\dfrac{3}{2u_d}(K_{pP} + \dfrac{K_{pI}}{s})(Q_{ref} - Q) \end{cases} \tag{25}$$

In Formula (25), K_{pP} represents the proportional regulation gain, while K_{pI} denotes the integral regulation gain associated with the power outer loop. The photovoltaic system produces two types of power: P (active power) and Q (reactive power). Within the framework of the energy storage system, i_{dref} and i_{qref} signify the reference values for the d-axis and q-axis, respectively. For a visual representation of these concepts, please refer to Figure 9, which depicts the control block schematic.

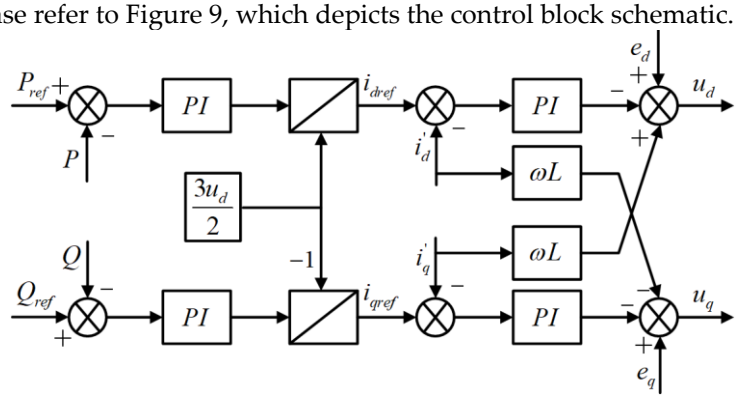

Figure 9. Power outer loop current inner loop control block diagram.

In photovoltaic energy storage systems, the energy storage mechanism utilizes a dual closed-loop control strategy, which comprises an outer power loop and an inner current loop. The control methodology for the inner current loop is analogous to that employed in the inner current loop of the photovoltaic system. Likewise, the control principle governing the outer power loop is consistent with that of the voltage outer loop in the photovoltaic system; thus, a detailed analysis of this aspect is unnecessary. The parameters for

the inner current loop can be established through the following calculations: $K_{pp} = 0.01$ and $K_{pI} = 0.5$.

4.4. Inverter Control Strategy of Energy Storage Systems Under Off-Grid Operation Mode

In light of the discontinuation of voltage and frequency support from the grid, it is imperative for the inverter to implement a constant voltage and constant frequency (V/F) control strategy to operate effectively in an off-grid mode. The V/F control methodology utilized by the energy storage system is based on a double closed-loop decoupling control mechanism and the inverse Park coordinate transformation. The primary aim of this approach is to provide the system with a stable reference for both voltage and frequency.

The segregation of voltage and current enables dual closed-loop regulation of these parameters. Reference values for both voltage and frequency are established. When outputs u_d and u_q from the current inner loop function as modulation signals, output u_d and u_q are modified to enhance the dynamic response characteristics of the system and to optimize the performance of the existing inner loop. The methodology for determining the reference value of the electric ring differs between V/F control and P/Q control.

The state equation, which is constructed using the voltage across the capacitor as the state variable, can be derived in the following manner:

$$\begin{cases} C_4 \dfrac{du_d}{dt} = i_{dL_3} - \omega_{ref} C_4 u_q - i_{dl} \\ C_4 \dfrac{du_q}{dt} = i_{qL_3} - \omega_{ref} C_4 u_d - i_{ql} \end{cases} \tag{26}$$

In Formula (26), the variable C_4 denotes the filter capacitor, while u_d and u_q represent the components of the output voltage from the battery inverter associated with the d- and q-axes, respectively. The variable ω_{ref} signifies the angular frequency of the grid. Furthermore, i_{dL_3} and i_{qL_3} indicate the d-axis and q-axis components of the filter inductor current, respectively. Additionally, i_{dl} and i_{ql} represent the d-axis and q-axis components of the output current from the battery inverter, respectively. Formula (26) serves as the foundation for deriving the governing equation of the voltage outer loop.

$$\begin{cases} i_{dref} = \left(K_p + \dfrac{K_i}{s} \right) \left(u_{dref} - u_d \right) - \omega_{ref} C u_q + i_{dl} \\ i_{qref} = \left(K_p + \dfrac{K_i}{s} \right) \left(u_{qref} - u_q \right) + \omega_{ref} C u_q + i_{ql} \end{cases} \tag{27}$$

In Formula (27), the integral gain associated with the voltage outer loop is denoted by K_i, while the proportional gain is represented by K_P. The parameters u_{dref} and u_{qref} correspond to the standard values for the d-axis and q-axis, respectively, of the output voltage from the battery inverter.

The block diagram representing V/F control is depicted in Figure 10.

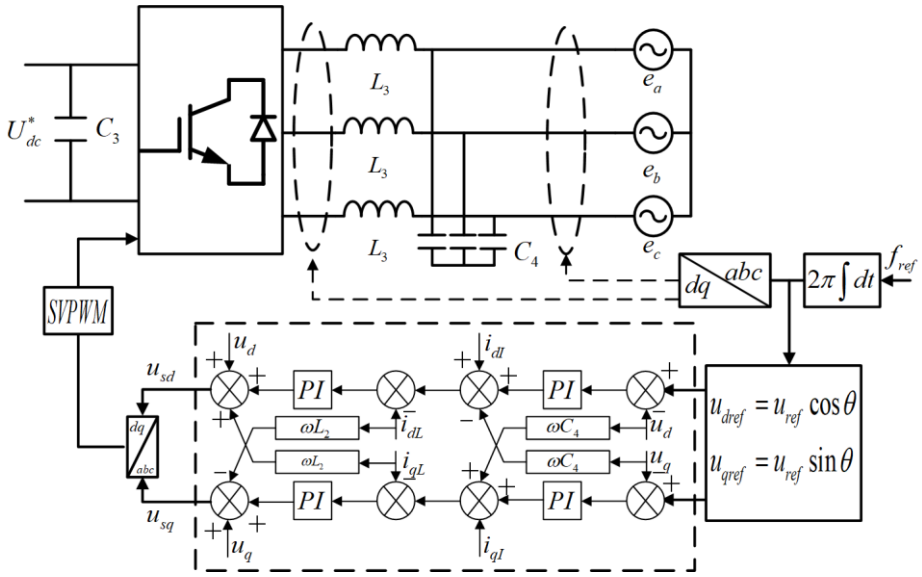

Figure 10. Schematic representation of an energy storage system operating independently of a power grid.

The investigation and analysis of the V/F control strategy for the energy storage system produced the following results regarding the proportional and integral gains of the voltage outer loop: 3 and 8, respectively. Furthermore, the proportional and integral gains for the current inner loop were established as 95 and 100.

5. Energy Storage Inverter's Smooth Switching Control Method

The control methodology for the energy storage battery inverter shifts from PQ control to V/F control when the microgrid transitions from a grid-connected state to an islanded state. In preparation for this transition, the inverter initially employs PQ control while preserving its current inner loop control mode. i_{dref} and i_{qref} are calculated by power. In order to switch to V/F control, the voltage outer loop takes the voltage reference signals u_{dref} and u_{qref} and uses them to determine the reference value of the current inner loop of the converter. This process necessitates a considerable investment of time and induces a sudden shift in correlation during the transition, as the existing control module functions under different input parameters. The application of a conventional PI regulator leads to an instantaneous modification of the current reference, thereby subjecting the energy storage converter to significant transient stress. This scenario not only threatens the safe operation of the system but also undermines the stability of the bus voltage. To address these challenges, we performed a comparative analysis of the architectures of grid-connected and off-grid controllers. Our analysis suggests that they function within the same current cycle, which allows us to enhance their control structure, as demonstrated in Figure 11.

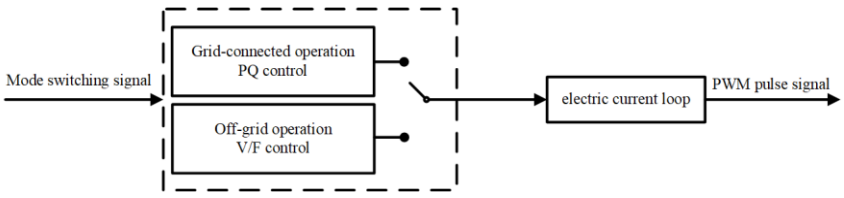

Figure 11. Operation mode control strategy improvement diagram.

Transitioning from a grid-connected system to an off-grid configuration necessitates modifications exclusively to the outer ring, while the inner ring maintains its operation in a shared capacity. To ensure that the input command of the current control module closely

approximates the value prior to the transition, it is essential to minimize fluctuations during the mode-switching process. In this context, when the system operates in an off-grid mode, the d-axis current reference value denoted as i_{dref1}, which is derived from constant power control based on active and reactive power (PQ) principles, is utilized alongside the current reference value denoted as i_{dref2} generated by compensation and V/F control. This integration results in a new current reference value denoted as i_{dref}. A comparable methodology can be employed to derive the q-axis current, as outlined below:

$$i_{dref} = i_{dref1} + i_{dref2} \tag{28}$$

$$i_{qref} = i_{qref1} + i_{qref2} \tag{29}$$

In a similar context, following the deactivation of the grid, the existing inner control loop can be optimized with enhanced effectiveness. u_d and u_q are utilized as voltage feedforward compensation during the generation of the voltage signal by the inner loop. This methodology aims to alleviate the transient effects linked to the switching process and to compensate for the slow dynamic response of the outer voltage control loop.

$$u_{sd} = u_{dref1} + u_{dref2} \tag{30}$$

$$u_{sq} = u_{qref1} + u_{qref2} \tag{31}$$

The following Figure 12 depicts the off-grid switching controller for the battery.

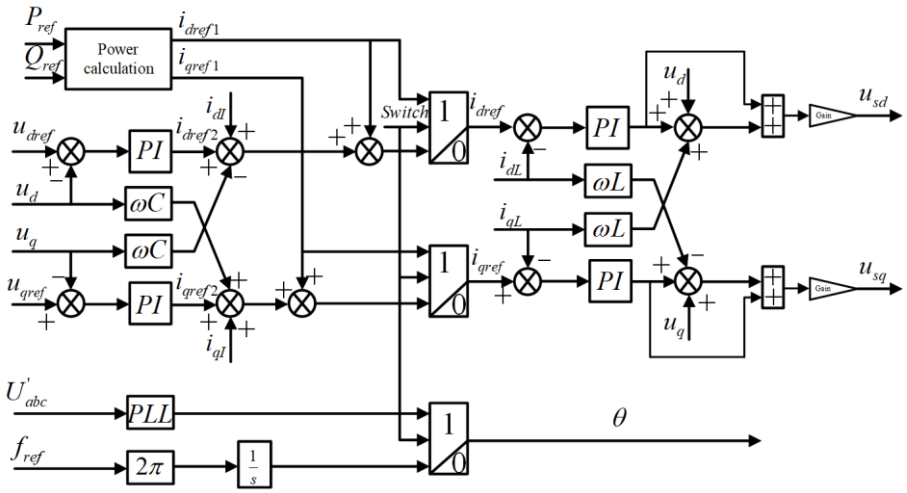

Figure 12. Energy storage system and off-grid switching control block diagram.

As depicted in Figure 12, operations that are connected to the grid are represented by the value of 1, while operations that are off-grid are indicated by the value of 0.

When the switching signal is activated to a value of 1, the system functions in grid-connected mode. At this juncture, the input for the current inner loop comprises currents i_{dref1} and i_{qref1}, which are obtained from power calculations based on the designated power reference value. The phase information at this stage is acquired through the phase-locked loop.

When the switching signal is set to zero, the system functions in off-grid mode. The inner current control loop employs a newly computed current reference value, which has been modified through the application of Formulas (28) and (29). The phase information is obtained from V/F control.

6. Simulation Analysis and Experimental Verification

6.1. Simulation Analysis

A simulation model of a photovoltaic energy storage system, as depicted in Figure 13, was developed utilizing MATLAB/Simulink to examine the feasibility of seamless power transition between grid-connected and off-grid modes. Parameter settings are as follows: The frequency f is 50 Hz, the critical load is 4000 W, the grid side filter inductance of the battery is 2.5×10^{-2} H, and the filter capacitance is 2×10^{-5} F. The PV side filter inductance is 2.1×10^{-2} H.

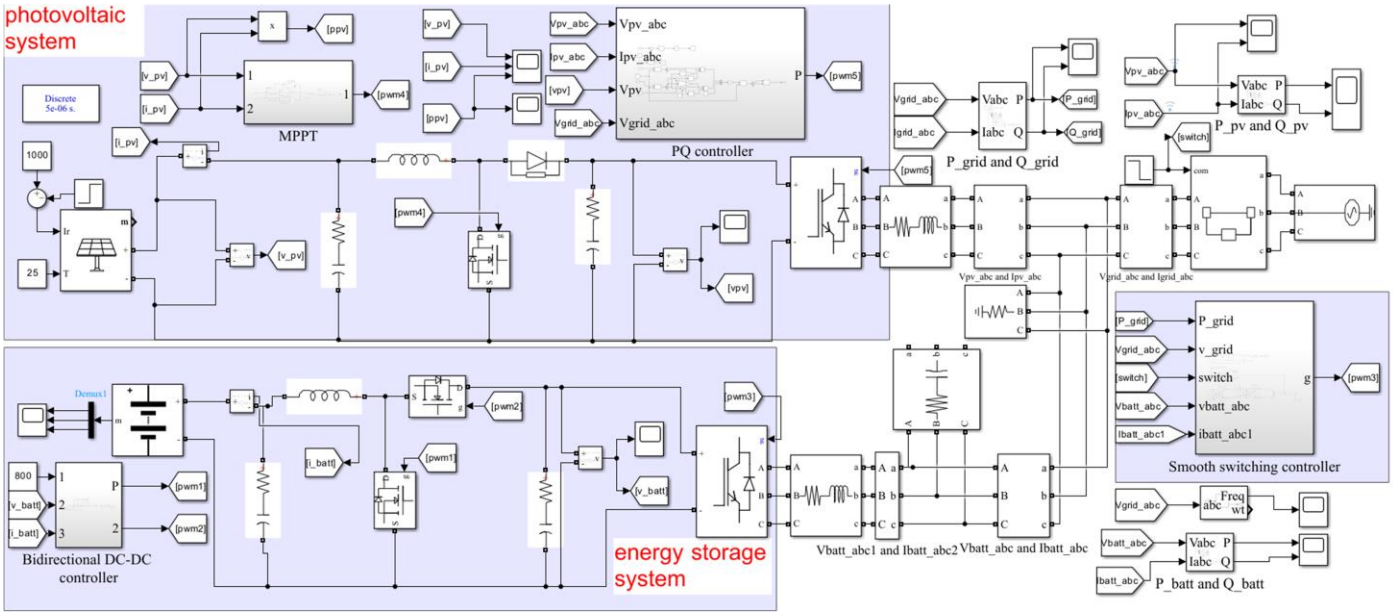

Figure 13. Photovoltaic energy storage system and off-grid simulation model.

An analysis of Figure 14a,b indicates that the photovoltaic system, which functions as the primary power source, undergoes considerable power fluctuations due to variations in light intensity. In comparison, the influence of temperature changes on power fluctuations is comparatively minimal. Therefore, this study maintains a constant temperature for the photovoltaic panels while ensuring a stable connection to the power grid by modulating light intensity. The curve depicting the variations in light intensity employed in this research is presented in Figure 14c.

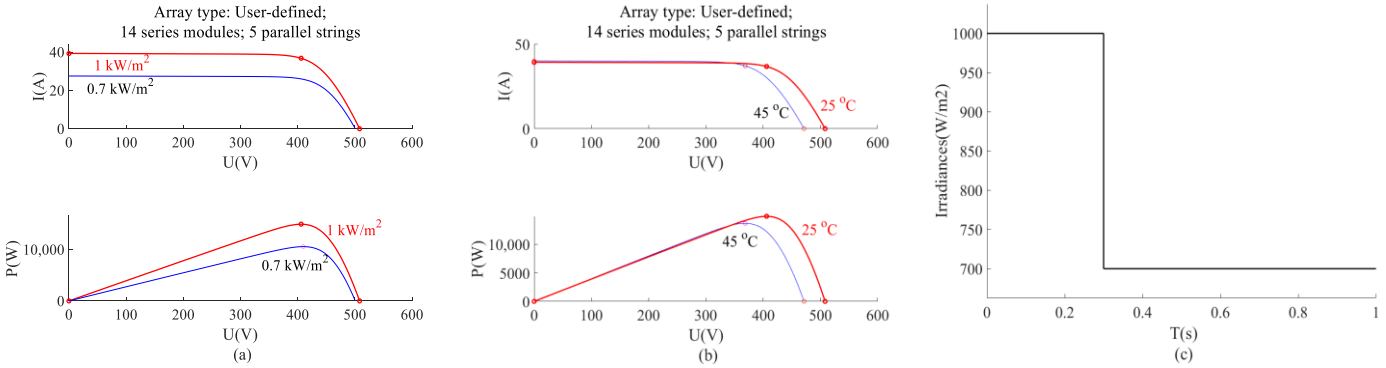

Figure 14. The power curves of photovoltaic panels under different light intensities and different temperatures and the light intensity curves adopted in this paper. (**a**) At a constant temperature, the output power curve of the photovoltaic panel obtained by changing the light intensity is obtained. (**b**) The output power curve of the photovoltaic panel is obtained by changing the temperature under constant light intensity. (**c**) The light intensity change curve adopted in this paper.

In order to conduct a comprehensive analysis of the variations in current and voltage during both grid-connected and off-grid operations of the photovoltaic energy storage

system illustrated in Figure 13, this study extends the simulation duration to 1 s and categorizes the process into three distinct stages for detailed examination. Throughout the simulation, the temperature of the photovoltaic panel is consistently maintained at 25 °C, while system variations are assessed by altering the light intensity. The initial stage establishes a light intensity of 1000 W/m². In the second stage, the light intensity is reduced to 700 W/m² at 0.3 s. The final stage represents the off-grid operation phase, which commences at 0.6 s, during which the photovoltaic energy storage system is disconnected from the power grid and continues to operate at a light intensity of 700 W/m². The energy storage component employed is a battery, characterized by an initial state of charge of 80%, a rated capacity of 200 Ah, and a rated voltage of 400 V. The system is connected to the grid with a constant power output of 10,000 W, and the reactive power is maintained at Q = 0 Var, ensuring operation with a unit power factor to comply with grid connection standards. The transition from grid-connected to off-grid operation can be achieved through two primary methods: active off-grid and passive off-grid systems, with this article primarily focusing on active off-grid systems.

Figure 15 depicts the current and voltage waveforms on the grid side during operation while connected to the grid.

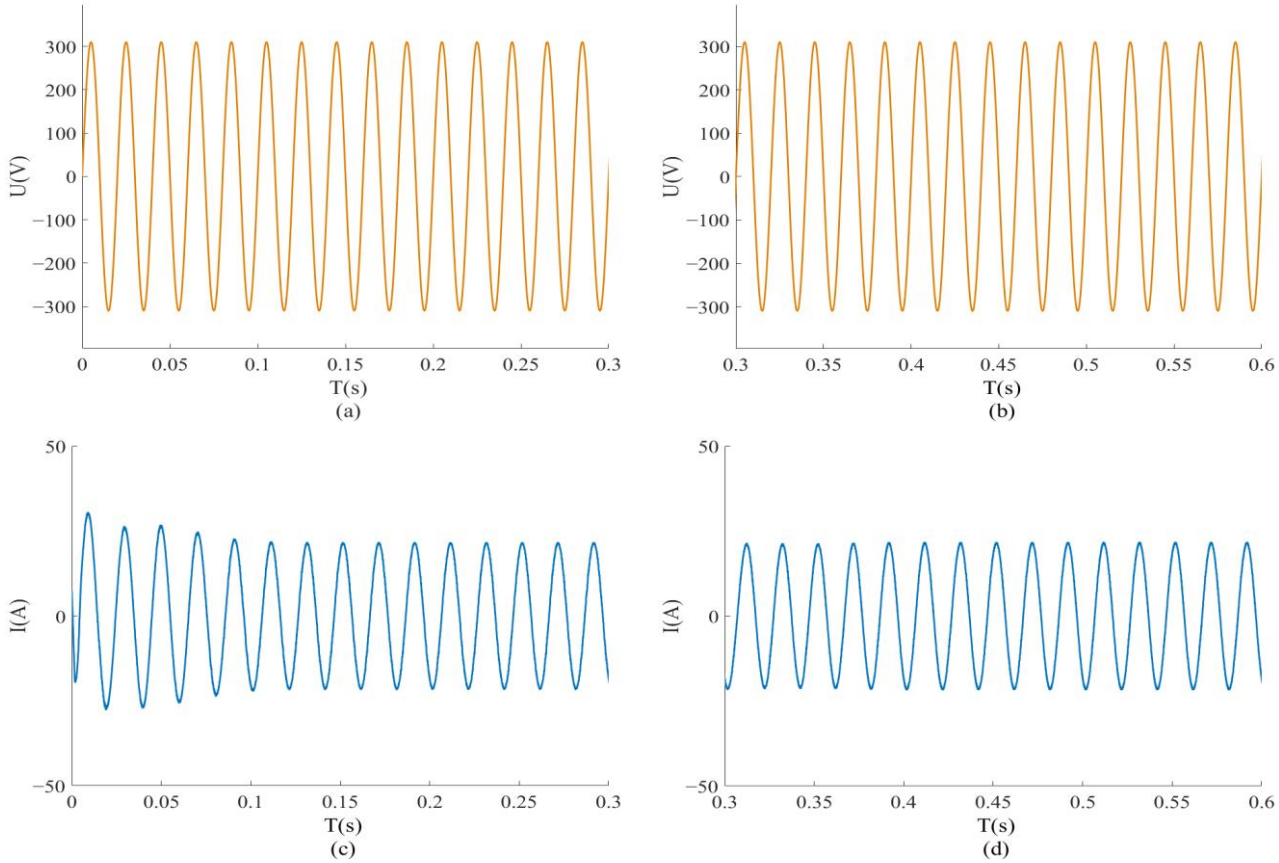

Figure 15. Grid-side a-phase voltage and current waveform. (**a**) The voltage waveform of the a-phase on the grid side when the light intensity does not change. (**b**) A-phase voltage waveform on the grid side when the light intensity changes. (**c**) The a-phase current waveform on the grid side when the light intensity does not change. (**d**) The a-phase current waveform on the grid side when the light intensity changes.

The analysis presented in Figure 15 demonstrates that the current and voltage waveforms on the grid side exhibit sinusoidal characteristics and maintain a high degree of stability throughout the operational period, with no significant distortion or current surges observed. Initially, the system achieves stabilization within 0.07 s, resulting in

consistent current and voltage on the grid side in terms of both frequency and phase. However, at 0.3 s, a variation in light intensity results in insufficient output power from the photovoltaic system for grid connection. Importantly, the energy storage battery ensures the constancy of the grid side current and voltage during this interval. The findings indicate that the energy storage battery plays a critical role in maintaining stable current and voltage levels when the photovoltaic system is integrated with the grid, thereby significantly mitigating output fluctuations that arise from variations in light intensity. The power simulation waveform corresponding to the system's connection to the grid is illustrated in Figure 16.

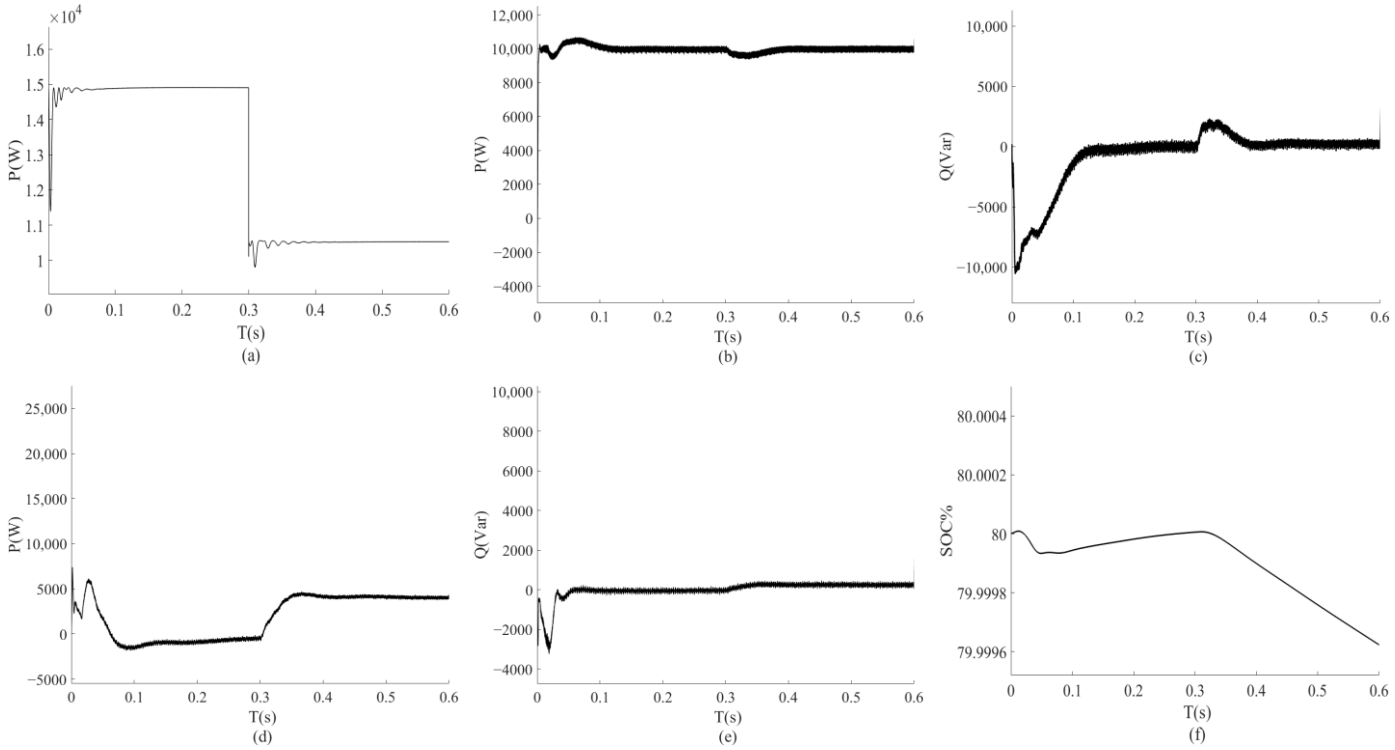

Figure 16. System power simulation diagram. (**a**) Output power waveform of the photovoltaic system. (**b**) Output active power waveform of the grid side. (**c**) The grid side output reactive power waveform. (**d**) Energy storage battery output active power waveform. (**e**) Energy storage battery output reactive power waveform. (**f**) State of charge waveform of the energy storage battery in grid-connected mode.

To ensure a stable power output, this research presents a power control strategy for photovoltaic energy storage systems that utilizes PQ control. In the first stage, the photovoltaic system reaches a steady output of 14,900 W after 0.04 s, with a measured light intensity of 1000 W/m^2. The light intensity reaches 700 W/m^2 at 0.3 s; the system stabilizes under the new conditions at 0.07 s; and the output power is 10,525 W afterward. The energy storage battery needs to make up for the power loss in the system since, due to important loads, the output power of the photovoltaic panels is higher than the grid-connected power before 0.3 s but lower afterward. The battery's state of charge is increased by 900 W for 0.3 s, as shown in Figure 16d–f. Then, after 0.3 s, the state of charge is decreased by 3475 W, as shown in Figure 16d,e.

Figure 17 presents the results of the Fast Fourier Transform (FFT) analysis conducted on the grid-connected current.

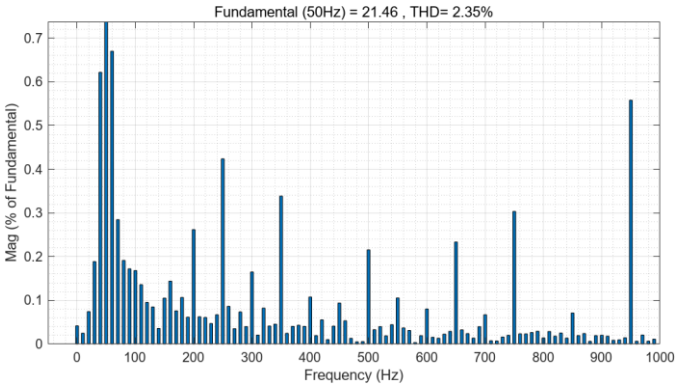

Figure 17. Analysis of grid-connected current using the Fourier Transform.

In the context of the grid-connected operation of the photovoltaic energy storage system, the total harmonic distortion (THD) of the grid-connected current is measured at 2.35% under stable conditions. This THD value is below the regulatory threshold of 5%, thereby meeting the requirements for grid connection. Furthermore, the fundamental frequency of the signal is identified as 50 Hz, with a corresponding magnitude of 21.46.

The disconnection from the power grid in the photovoltaic energy storage system occurs at 0.6 s. To maintain stable voltage and frequency, the energy storage system has recently integrated seamless switching technology. The photovoltaic system consistently delivers 10,500 W of power to the critical load and batteries. The energy storage battery is designed to absorb surplus power, thereby aiding in the stabilization of system frequency and voltage, as illustrated in Figure 18a. Additionally, the state of charge of the energy storage battery is observed to be increasing, as depicted in Figure 18b, while its power absorption capacity is recorded at 6,000 W, as shown in Figure 18c.

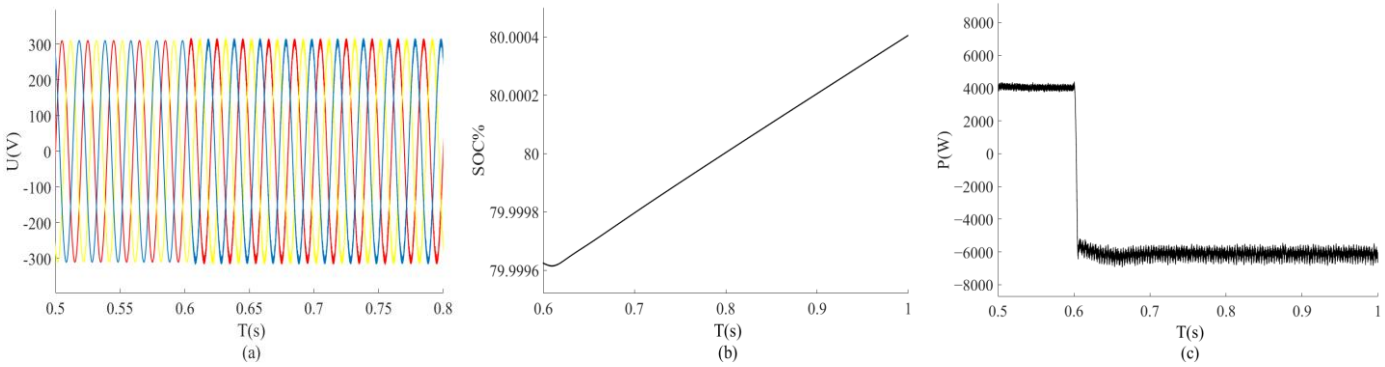

Figure 18. Current on the AC bus, voltage at the battery, and power output spectrum. (**a**) AC bus waveform. (**b**) State of charge waveform of battery. (**c**) Active power waveform of battery output.

The system's frequency exhibits substantial fluctuations at 0.6 s following the off-grid operation. To achieve a state of seamless switching in an energy storage system, the system frequency deviation is about $\Delta \approx 0.04$ Hz. As shown in Figure 19a, the frequency deviation of the microgrid before and after switching is not more than 0.1% f_n. When conventional switching is adopted, the frequency deviation is about $\Delta \approx 0.2$ Hz, as shown in Figure 19b, which significantly exceeds this threshold and fails to meet the requirements of microgrid frequency stability. The single-phase current output by smooth switching and conventional switching AC bus is shown in Figure 19c,d. The current waveform of the smooth switching control strategy exhibits no significant fluctuations and gradually approaches zero within 0.005 s. There is no substantial current spike.

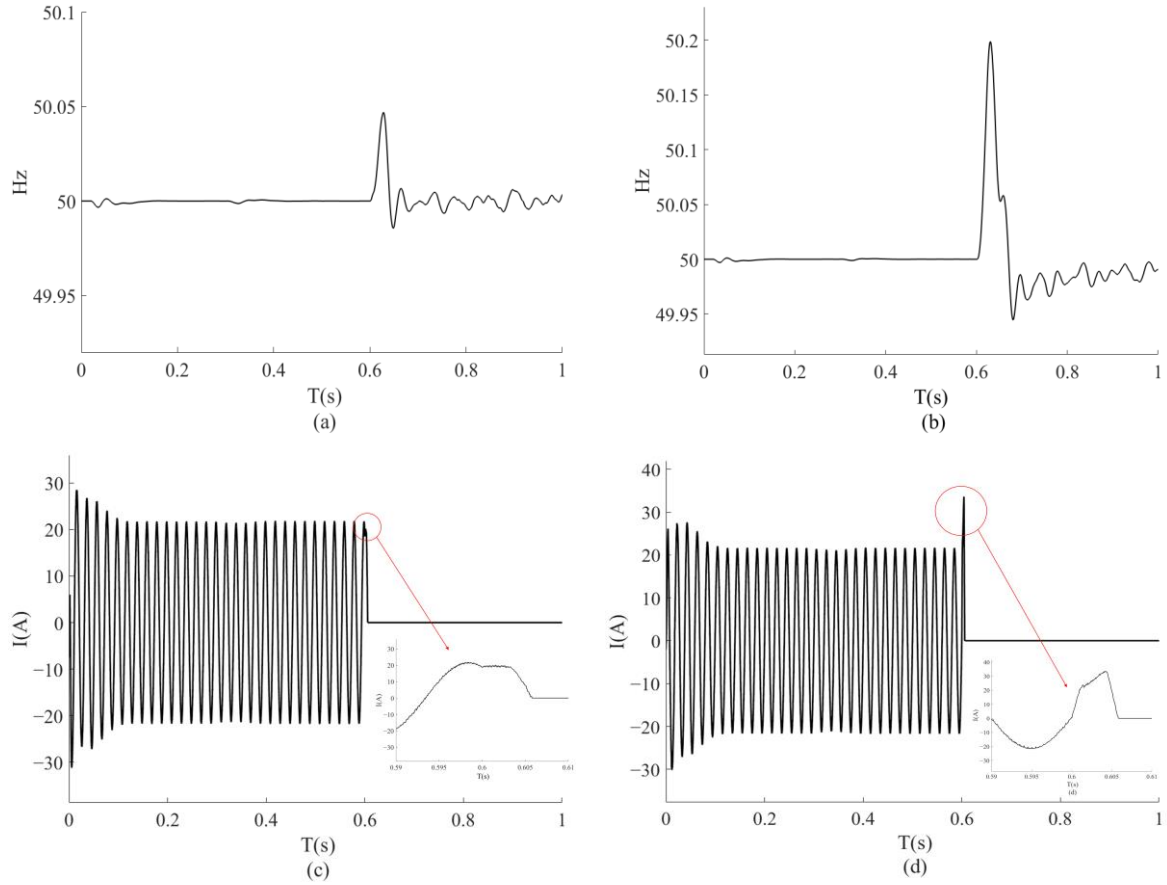

Figure 19. AC bus frequency and current waveform. (**a**) The smooth switching AC bus frequency waveform is adopted. (**b**) The conventional switching AC bus frequency waveform is adopted. (**c**) The smooth switching control strategy is adopted to control the AC bus current waveform and local amplification diagram. (**d**) The conventional switching control strategy is used to control the AC bus current waveform and local amplification diagram.

The output current waveform of the energy storage side is shown in Figure 20.

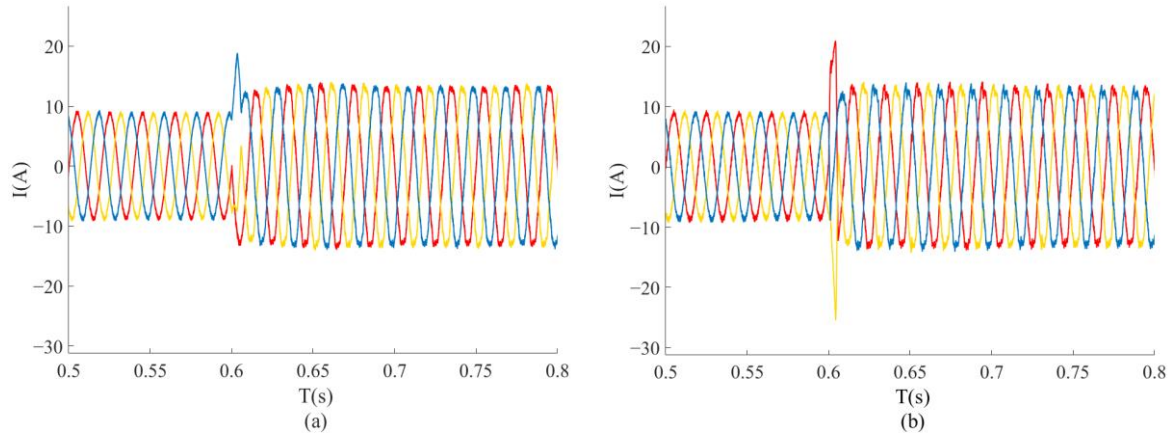

Figure 20. Electrical current waveform diagram of an energy storage battery's output. (**a**) The smooth switching energy storage battery output current waveform diagram is adopted. (**b**) The output current waveform of the conventional switching energy storage battery is used.

The implementation of smooth switching markedly reduces the current surge experienced during the transition from grid-connected to off-grid operation. Specifically, the current variation is approximately 4 A, whereas conventional switching methods result in

a current surge of 15 A. Additionally, the frequency variation associated with this transition is approximately 0.04 Hz. In Table 1, by comparing with [24], the smooth switching control strategy can reduce the impact of voltage and current frequency on the system.

Table 1. Comparison of voltage, current, and frequency deviation under different control strategies.

Attribute	Improved Smooth Switching	Conventional Smooth Switching	Control Strategy for Smooth Switching Between Island Operation Mode and Grid-Connection Operation Mode of Microgrid [24]
U(V)	3.2%	4.8%	22%
I(A)	26%	66%	80%
Frequency	0.04 Hz	0.2 Hz	0.3 Hz

Figure 21 illustrates the output voltage of the DC side of the photovoltaic energy storage system. Initially, the two waveforms exhibited stability for approximately 0.1 s following the emergence of the overshoot phenomenon. As the output of the photovoltaic system has not yet attained maximum power, the battery must compensate for the deficit, the external discharge of the battery currently reduces the DC bus voltage below its rated level. As light intensity diminishes, the DC bus voltage correspondingly declines. After 0.6 s, the photovoltaic output power is entirely directed to the battery, leading to an increase in the DC bus voltage. However, within approximately 0.1 s, the voltage of the entire system exhibits progressive stabilization, maintaining a voltage level of 800 V.

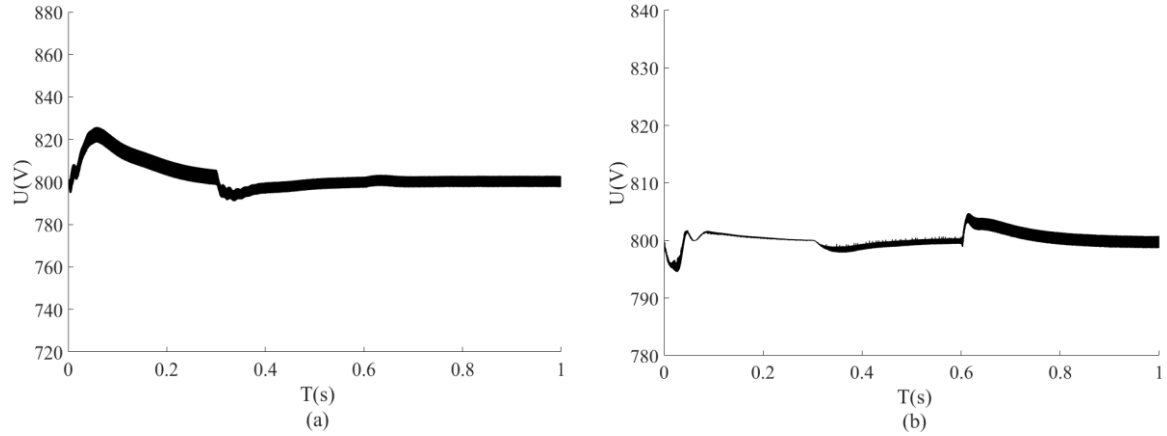

Figure 21. DC-side voltage curve of the photovoltaic energy storage system. (**a**) DC-side voltage waveform of the photovoltaic system. (**b**) DC-side voltage waveform of the energy storage system.

6.2. Experimental Verification

The seamless switching control strategy of photovoltaic energy storage grid-connected and grid-connected to off-grid mentioned in this paper is verified by experiments. In the experiment, the output fluctuation in the photovoltaic system is simulated by controlling the light intensity, and the switching between grid-connected and off-grid is realized by disconnecting the switch at PCC. The detailed results of these experiments are presented in Figure 22.

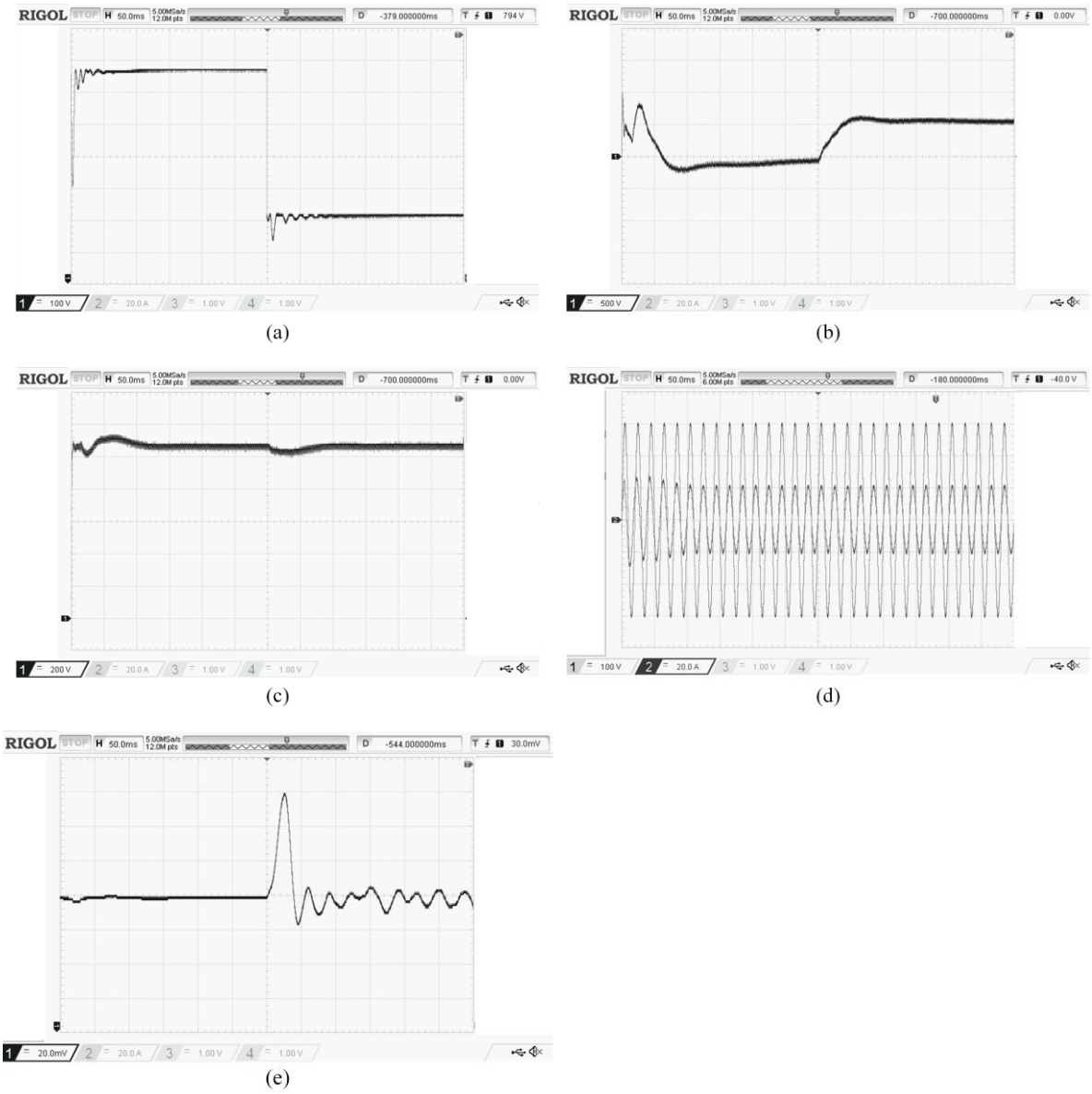

Figure 22. The experimental waveform of the control strategy proposed in this paper. (**a**) Photovoltaic output power waveform. (**b**) Energy storage output power waveform. (**c**) Grid-connected power waveform. (**d**) Phase a voltage and current waveform at PCC. (**e**) Frequency waveform at PCC.

7. Discussion

Simulation results indicate that transitioning the photovoltaic energy storage system from a grid-connected configuration to an off-grid setup results in a frequency fluctuation of approximately 0.04 Hz. Furthermore, the frequency can be stabilized at 50 Hz within approximately 0.05 s through a smooth switching process. In comparison to traditional switching methods, this approach exhibits reduced frequency fluctuations and a shorter recovery time. This ensures that the frequency deviation before and after off-grid switching does not exceed the specified threshold of $0.1\% f_n$. This method results in a decrease in current fluctuation of approximately 10 A relative to conventional switching techniques.

Experimental validation indicates that the photovoltaic system consistently delivers maximum power output in response to variations in light intensity. Furthermore, the energy storage battery effectively provides a buffering mechanism, facilitating a stable power connection to the grid. During the transition from grid-connected to off-grid

operation, the implemented smooth switching control strategy ensures that frequency fluctuations remain within permissible limits, thereby preventing any adverse effects throughout the switching process. Consequently, both bus current and voltage maintain stability, resulting in seamless transitions between operational modes.

Drawing upon the theoretical analysis and simulation validation presented previously, this study adopts a more straightforward methodology for maximum power point tracking in solar energy systems through the use of conductance increments, as opposed to developing a more sophisticated control mechanism. While the analysis addresses the transition from off-grid to grid-connected solar energy storage systems, it does not explore the reverse transition from grid-connected to off-grid systems. Additionally, this article does not engage in a comprehensive examination of the harmonic issues associated with the power grid; rather, it merely affirms the feasibility of the overall system control strategy and utilizes L-type and LC-type filters as a rudimentary solution. In light of the limitations identified in this paper and the potential advancements in solar energy storage systems, the authors intend to undertake extensive research and engage in detailed discussions on the following topics:

1. The maximum power point tracking problem of photovoltaic systems under partial shading is analyzed and verified to achieve tracking accuracy in more complex situations.
2. The transformation from off-grid to grid-connected is analyzed in detail. At the same time, a pre-synchronization structure is added to reduce the phase or amplitude difference when the system is converted from the island to the grid to achieve a smooth grid connection.
3. In order to reduce the high-order harmonics in the grid-connected mode and reduce the total harmonic distortion rate of the grid-connected current, a more advanced three-level grid-connected inverter is adopted.
4. A more advanced virtual synchronous generator control strategy is adopted to improve the service life of the energy storage system, reduce the impact on the power grid, and increase the type and number of energy storage units.

8. Conclusions

In this study, the two control strategies of constant power grid-connected and grid-connected off-grid switching of photovoltaic energy storage microgrids are simulated and experimentally verified. The bidirectional DC / DC converter and three-phase voltage source PWM converter of the system are mainly studied. This research summarizes the mathematical modeling process, system topology, operation mode, and control strategy adopted. When the microgrid fails, it is quickly isolated from the main grid, and the reasons for the temporary effect during the switching process are explored. Based on the control strategy before and after switching, the current inner loop of PQ control is combined with the current inner loop of V / F control to realize the common use of the current inner loop, and the reference voltage output by the current inner loop is compensated. Simultaneously, the present reference value of the voltage outer loop output is adjusted to mitigate the impact of discrepancies in the reference current on the controller during the switching process. A detailed flowchart illustrating the operation of a photovoltaic energy storage microgrid transitioning between grid-connected and off-grid modes is presented, followed by the execution of a simulation experiment. The results of the simulation indicate that the transition of the photovoltaic energy storage microgrid from grid-connected to off-grid mode does not result in significant transient disturbances, enhances power quality, and ensures the continuous charging of electric vehicles as well as the stable operation of critical system loads. The effectiveness of the seamless switching control method for photovoltaic energy storage microgrids has been validated.

Author Contributions: Conceptualization, T.W.; software, writing—original draft preparation, and writing—review and editing, J.M.; formal analysis, C.L.; investigation, X.L. and S.C.; validation J.Z.; All authors have read and agreed to the published version of the manuscript.

Funding: This research received no external funding.

Data Availability Statement: The original contributions presented in the study are included in the article, further inquiries can be directed to the corresponding author.

Conflicts of Interest: The authors declare no conflicts of interest.

Nomenclature

U_{PV}	Photovoltaic panel output voltage
E_{bat}	Output voltage of energy storage battery
r_1	Internal resistance of photovoltaic panel
r_2	Internal resistance of energy storage battery
$T_1 \sim T_{12}$	Power switches
$V_{13} \sim V_{15}$	DC-side power switch tube
$C \quad C_1 \quad C_2 \quad C_3 \quad C_4$	Smoothing capacitance
$L \quad L_1 \quad L_2 \quad L_3$	Filter inductance
P_{pv}	Photovoltaic side output power
P_{bat}	Energy storage battery side output power
P_{grid}	Grid output power
P_{load}	Load consumption power
$K_{iP} \quad K_{iI}$	The proportional gain and integral gain of the current inner loop
$K_{vP} \quad K_{vI}$	Proportional gain and integral gain of voltage outer loop
$K_{pP} \quad K_{pI}$	The proportional gain and integral gain of the power loop

References

1. Chen Yang, N.; Liang, J.; Ding, L. Integrated Optical Storage Charging Considering Reconstruction Expansion and Safety Efficiency Cost. *Power Syst. Technol.* **2023**, *47*, 3557–3569.
2. Wang, T.; Lin, C.; Zheng, K.; Zhao, W.; Wang, X. Research on Grid-Connected Control Strategy of Photovoltaic (PV) Energy Storage Based on Constant Power Operation. *Energies* **2023**, *16*, 8056.
3. Zhao, J.; Gao, T.; Zhang, W. Black-start control strategy of optical storage microgrid based on improved V/f control and virtual oscillator. *Electron. Meas. Technol.* **2023**, *46*, 7–15.
4. Kim, H.M.; Kinoshita, T. A multiagent system for microgrid operation in the grid-interconnected mode. *J. Electr. Eng. Technol.* **2010**, *5*, 246–254.
5. Wang, T.; An, J.; Wang, Z. Microgrid optical storage multi-source coordination and multi-mode smooth switching control. *Power Electron.* **2023**, *57*, 99–103.
6. Song, D.; Zhang, W.; Wang, C. Energy coordination control strategy of microgrid with optical storage system. *J. Harbin Univ. Sci. Technol.* **2021**, *26*, 94–103.
7. Pei, W.; Li, S.; Li, H.; Tang, X.; Zuo, W. Key technology and testbed for microgrid operation control. *Autom. Electr. Power Syst.* **2010**, *34*, 94–96.
8. Wang, C.; Liu, M.; Guo, L. Cooperative operation and optimal design for islanded microgrid. In Proceedings of the 2012 IEEE PES Innovative Smart Grid Technologies (ISGT), Washington, DC, USA, 16–20 January 2012.
9. Pogaku, N.; Prodanovic, M.; Green, T.C. Modeling, analysis and testing of autonomous operation of an inverter-based microgrid. *IEEE Trans. Power Electron.* **2007**, *22*, 613–625.
10. Wang, C.; Li, X.; Guo, L.; Li, Y. A seamless operation mode transition control strategy for a microgrid based on master-slave control. *Sci. China Technol. Sci.* **2012**, *55*, 11.

11. Wang, T.; Li, X.; Zhang, J.; Chen, S.; Ma, J.; Lin, C. Fractional Sliding Mode Observer Control Strategy for Three-Phase PWM Rectifier. *World Electr. Veh. J.* **2024**, *15*, 316.
12. Jiang, J.D.; Lu-Xia, L.; Cai, S.J.; Ke-Yong, H. Research of droop control strategy for parallel operation of multi-inverters in microgrid. *J. Zhejiang Univ. Technol.* **2014**, *42*, 132–136+161.
13. Tian, L.; Tang, Z.; Tian, C. Research on smooth switching of microgrid based on state follower. *Power Syst. Technol.* **2017**, *41*, 1285–1290.
14. Xu, G. Research on coordinated optimization strategy of photovoltaic and energy storage combined smart microgrid based on hierarchical control. *Acta Energiae Solaris Sin.* **2024**, *45*, 111–120.
15. Chen, J.W.; Zhang, R.; Zhang, D.; Meng, Y.J. Research of optical storage DC micro-grid inverter. *J. Shaanxi Univ. Sci. Technol.* **2017**.
16. Pan, G.; Zeng, D.; Wang, G. Fault Analysis on Distribution Network with Inverter Interfaced Distributed Generations Based on PQ Control Strategy. *Proc. Csee* **2014**, *34*, 555–561.
17. Mortezaei, A.; Lute, C.; Simoes, M.G.; Marafao, F.P.; Boglia, A. PQ, DQ and CPT control methods for shunt active compensators — A comparative study. In Proceedings of the 2014 IEEE Energy Conversion Congress and Exposition (ECCE), Pittsburgh, PA, USA, 14–18 September 2014.
18. Wang, A.; Cai, Z.; Mu, X. Research on asynchronous island mode switching strategy of partitioned interconnected distribution network. *Power Syst. Clean Energy* **2024**, *40*, 59–69.
19. Zhang, W.; Li, M.; Ren, W. Research on improved pre-synchronization control and off-grid switching strategy of microgrid based on optical storage control. *Electron. Meas. Technol.* **2022**, *45*, 8–14.
20. Zhou, L.; Ren, Y.; Chen, Q. Research on operation control strategy of new master-slave control microgrid. *Renew. Energy Resour.* **2021**, *39*, 1100–1106.
21. Bi, D.; Zhou, W.; Dai, Y. Seamless switching strategy of energy storage converter in AC / DC hybrid microgrid. *Autom. Electr. Power Syst.* **2016**, *40*, 84–89.
22. Chtita, S.; Derouich, A.; Ghzizal, A.E.; Motahhir, S. An improved control strategy for charging solar batteries in off-grid photovoltaic systems. *Sol. Energy* **2021**, *220*, 927–941.
23. Zhang, C.; Xu, J.; Zong, H. Master-slave structure microgrid inverter off-grid whole process smooth switching control strategy. *Autom. Electr. Power Syst.* **2022**, *46*, 125–133.
24. Yang, Y.; Yang, K.; Shao, Y. Research on grid-connected and off-grid smooth switching control strategy of microgrid. *Renew. Energy Resour.* **2018**, *36*, 36–42.
25. Xu, J.; Lu, W.; Wu, L. Grid-connected and off-grid smooth switching control of low-voltage microgrid inverter. *Sci. Technol. Eng.* **2017**, *17*, 36–43.
26. Chen, J.; Chen, X.; Feng, Z. Seamless switching control strategy for grid-connected/islanded operation mode of microgrid system. *Proc. CSEE* **2014**, *34*, 3089–3097.
27. Liu, M.; Wang, S.; Wen, S. Research on grid-connected and off-grid smooth switching control strategy of photovoltaic energy storage microgrid. *Renew. Energy Resour.* **2020**, *38*, 1633–1639.
28. Zheng, J.; Wang, Y.; Li, X. Control Methods and Strategies of Microgrid Smooth Switchover. *Autom. Electr. Power Syst.* **2017**, *35*, 17–24.
29. Battula, S.; Panda, A.K.; Garg, M. Stand-alone PV connected system with energy storage with flexible operation. *Electr. Eng.* **2024**, *106*, 2893–2907.
30. Cheng, Q.; Cheng, Y.; Zhang, L. Grid-connected/off-grid Switching Control Strategy of MMC-PET AC/DC Hybrid Microgrid. Based on Disturbance Observer. *High Volt. Eng.* **2024**, *50*, 1196–1204.
31. Luo, L.; Li, Y.; Li, Z. Microgrid based on Van der Pol oscillator and PQ control Grid-connected and off-grid coordinated control strategy. *Electr. Power Autom. Equip.* **2023**, *43*, 130–139.
32. Carvalho, F.S.; Lessa, F.T.; Silveira L M. Smart Protection System for Microgrids with Grid-Connected and Islanded Capabilities Based on an Adaptive Algorithm. *Energies* **2023**, *16*, 2273–2273.
33. Silveira, D.R.; Silva, D.A.S.; Sampaio, P.L. Full-order models and dynamic assessment of droop-controlled grid-connected and off-grid DC microgrids. *Sustain. Energy Technol. Assess.* **2024**, *64*, 103685.
34. Wang, T.; Zheng, K.; Liu, W. Research on charging and discharging control strategy of electric vehicle in vehicle-grid interaction mode. *Automob. Technol.* **2023**, 20–27. https://doi.org/10.19620/j.cnki.1000-3703.20230142.